Supporting Information

Ce-Doped Nanorod-like NiFe-MOF with Coordination Substitution Based on *In-situ* Co-Doping Method for Enhancing the Oxygen Evolution Reaction.

Xiao Wei, Shudi Yu, Jie Li, Tianpeng Liu, Shujin Li *, Shinichi Hata, Zhengying Wu *, Yukihide Shiraishi, Yukou Du *

College of Chemistry, Chemical Engineering and Materials Science, Soochow University, Suzhou 215123, PR China

School of Optical and Electronic Information, Suzhou City University, Suzhou 215104, PR China

** Corresponding author: Tel: 86-512-65880967, Fax: 86-512-65880089;*

E-mail: shujinli@suda.edu.cn; zywu@mail.usts.edu.cn; duyk@suda.edu.cn (Y. Du)

Experimental Section

1. Chemicals

Nickel(Ⅱ) nitrate ($Ni(NO_3)_2 \cdot 6H_2O$, AR, ⩾98.0%), potassium hydroxide (KOH, GR, ⩾85%), 1,4-terephthalic acid (1,4-H_2BDC, ⩾99.0%) were all produced by Sinopharm Chemical Reagent Co., Ltd. Ferric(Ⅲ) chloride ($FeCl_3 \cdot 6H_2O$, 99%), cerium(III) nitrate ($Ce(NO_3)_3 \cdot 6H_2O$, 99%), N, N-dimethylacetamide (DMAC, 99.0%) were all produced by MACKLIN Chemical Reagent Co., Ltd. Absolute ethanol (C_2H_5OH, AR, ⩾99.7%) was produced by Ling Feng Chemical Reagent Co., Ltd. Nafion ($C_{10}H_7OH$, 5 *wt*.%) was produced by Sigma-Aldrich Chemical Reagent Co., Ltd. All aqueous solutions were prepared using deionized water.

2. Preparation

2.1. Synthesis of Fe-MIL-53

1,4-H_2BDC (0.1 mmol, 16.6 mg) and $FeCl_3 \cdot 6H_2O$ (0.1 mmol, 27.0 mg) were added to 12 mL of DMAC in a Teflon vessel (20 mL). The mixture was stirred to form a yellow clear solution, transferred to a stainless-steel autoclave and then heated at 150 °C for 3 h. When cooled to room temperature, the products were collected via centrifugation and washed with ethanol and water for three times.

2.2. Synthesis of $Ni_{1.6}$Fe-MIL-53

The preparation process of $Ni_{1.6}$Fe-MIL-53 was the same as that of Fe-MIL-53, except that $Ni(NO_3)_2 \cdot 6H_2O$ (0.16 mmol, 46.6 mg) needs to be added to the solution at the beginning.

2.3. Synthesis of $CeNi_{1.6}$Fe-MIL-53

The preparation process of $CeNi_{1.6}$Fe-MIL-53 was the same as that of $Ni_{1.6}$Fe-MIL-53, except that $Ce(NO_3)_3 \cdot 6H_2O$ (0.1 mmol, 43.4 mg) needs to be added to the solution at the beginning.

2.4. Synthesis of Ce@$Ni_{1.6}$Fe-MIL-53

The first preparation process of Ce@$Ni_{1.6}$Fe-MIL-53 was the same as that of $Ni_{1.6}$Fe-MIL-53. Then the products were dispersed in ethanol, then $Ce(NO_3)_3 \cdot 6H_2O$ (0.1 mmol, 43.4 mg) was added into the above solvent, after ultrasonic dispersion, the mixture was remained reaction for 15 min at room temperature. The products were collected, washed with ethanol and water for three times, dried, and stored at room temperature.

2.5. Synthesis of $Ce_xNi_{1.6}$Fe-MIL-53 (x = 0.6, 0.8, 1.2, 1.4)

The preparation process of $Ce_xNi_{1.6}$Fe-MIL-53s was the same as that of $CeNi_{1.6}$Fe-MIL-53, except using different molar ratios of $Ce(NO_3)_3 \cdot 6H_2O$ (0.06 mmol, 0.08 mmol, 0.12 mmol and 0.14 mmol) at the beginning.

2.6. Synthesis of Ce_x@$Ni_{1.6}$Fe-MIL-53 (x = 0.6, 0.8, 1.2, 1.4)

The preparation process of Ce_x@$Ni_{1.6}$Fe-MIL-53 was the same as that of Ce@$Ni_{1.6}$Fe-MIL-53, except using different molar ratios of $Ce(NO_3)_3 \cdot 6H_2O$ (0.06 mmol, 0.08 mmol, 0.12 mmol and 0.14 mmol) at the second step.

3. Characterizations

Images were obtained using a JEM-2100 transmission electron microscope (TEM) produced by Hitachi in Japan. The materials' morphology and energy spectrum were analyzed using a Hitachi cold field emission scanning electron microscope (SEM) model S-400, which was connected with an energy dispersive spectrometer (EDS). The Talos field emission TEM was used to examine pictures of high-resolution TEM (HRTEM), high angle annular dark field scanning TEM (HAADF-STEM), and elemental mapping. Powder X-ray diffraction (XRD) patterns were analyzed using a Bruker D8 Advance diffractometer at 40 kV and 40 mA, using Cu Kα radiation (λ=1.5418 Å). X-ray photoelectron spectroscopy (XPS) data were collected using an EXCALAB 250 XI spectrometer with monochromatic Al Kα radiation as the excitation source. The C 1s peak binding energy (248.5 eV) was calibrated to ensure reliable results.

4. Electrochemical Tests

All electrochemical tests were performed on a CHI 660E electrochemical workstation produced by Chen Hua in China, using a three-electrode system in 1.0 M KOH solution. To create the electrochemical ink for testing, 2 mg of catalyst and 1 mg of conductive carbon black were distributed in 1 mL of ethanol, along with 10 μL of Nafion solution, and sonicated until completely dispersed. The ink was then dropped onto a polished glassy carbon (GC) electrode with a diameter of 5 mm and left to dry naturally at ambient temperature.

GC electrode was employed as the working electrode, carbon electrode was used as the counter electrode, while Hg/HgO(saturated KOH) electrode was utilized as the reference electrode. Linear sweep voltammetry (LSV) curves were collected at a scan rate of 5 mV s^{-1}. Corrected *IR* loss for all LSV curves. CP curve was operated at j = 10 mA cm^{-2} under the same conditions. The measured potential was corrected to RHE according to the formula: $E_{RHE} = E_{Hg/HgO} + 0.244V + 0.0592V \times pH$. Calculated the overpotential (η) according to the formula: $\eta = E_{RHE} - 1.23V$.

ECSA was determined using the electrochemical double-layer capacitance (C_{dl})

based on the formula: $ECSA = C_{dl}/C_s$ (C_s = 0.04 mF cm^{-2})[1], which calculated by testing the CV at different scan rates (v = 10 ~ 50 mV s^{-1}) in φ = 1.0 ~ 1.1 V vs RHE, based on the formula $C_{dl} = j_c/\nu$, where j_c is the charge current (mA cm^{-2}), and ν is the scan rate (mV s^{-1}).

The turnover frequency (TOF) of OER was calculated by the following equation:

$$TOF = \frac{j \times F}{16 \times RT \times C_{dl}}$$

where j is the current density at $\eta =$ 250 mV (mA cm^{-2}), F = 96580 C mol^{-1}, R = 8.314 J mol^{-1} K^{-1}, T is the absolute temperature (298 K), C_{dl} is the electrochemical double-layer capacitance (mF cm^{-2}).

EIS tests were recorded at 5 mV from 0.01 Hz to 10 kHz.

A two-electrode design was used in the overall water splitting examination. The GC electrode served as the anode, with commercial Pt/C as the cathode.

Proof Process Details of turnover frequency (*TOF*).

The turnover frequency (TOF) of OER was calculated by the following equation:

$$TOF = \frac{i}{n \times F \times N_{site}} = \frac{j \times A_{geo}}{n \times F \times N_{site}} \quad (1)$$

where j is the current density at an overpotential of 250 mV, A_{geo} is the geometric area of the electrode, n is the number of electrons involved (4 for OER), F is the Faraday constant (96580 C/mol), and N_{site} is the total number of metal sites on the electrode determined.

In above mentioned equation the total number of metal sites (N_{site}) can be determined from the value of slope (acquired from scan rate ν vs current i_c) [2].

$$slope = \frac{a^2 \times F^2 \times N_{site}}{4RT} = i_c/\nu = C_{dl} \times A_{geo}$$

The equation can be transformed as below:

$$N_{site} = C_{dl} \times A_{geo} \times \frac{4RT}{a^2 \times F^2} \quad (2)$$

Based on the equation (1) and (2), TOF can be calculated as below:

$$TOF = \frac{j \times A_{geo}}{n \times F \times N_{site}} = \frac{j \times A_{geo}}{4 \times F \times \left(C_{dl} \times A_{geo} \times \frac{4RT}{a^2 \times F^2} \right)} = \frac{j}{C_{dl} \times \frac{16RT}{a^2 \times F}} = \frac{j \times F \times a^2}{16 \times RT \times C_{dl}}$$

where j is the current density at an overpotential of 250 mV (mA cm^{-2}), F is the Faraday constant (96580 C/mol), R is the universal gas constant (8.314 J mol^{-1} K^{-1}), T is the absolute temperature (298 K), C_{dl} is the electrochemical double-layer capacitance (mF cm^{-2}), a^2 is the number of electron intricate in rate determining step (for oxidation process, suppose $a^2 = 1$).

$$\therefore TOF = \frac{j \times F}{16 \times RT \times C_{dl}}$$

Supporting Figures and Tables.

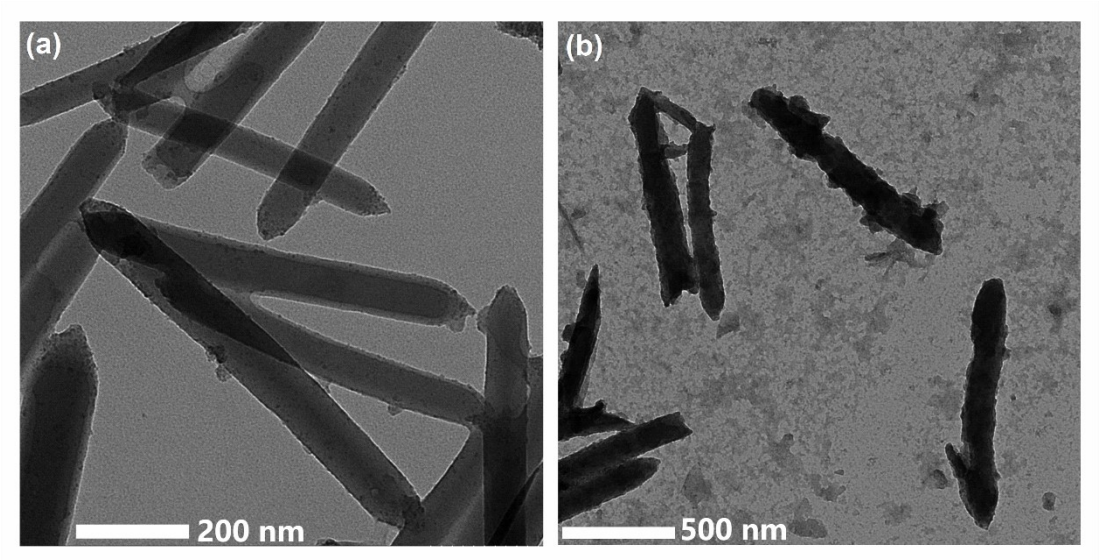

Fig S1. TEM images of (a) Fe-MIL-53 and (b) $Ni_{1.6}$Fe-MIL-53. Scale bars are: (a) 200 nm and (b) 500 nm resolutions.

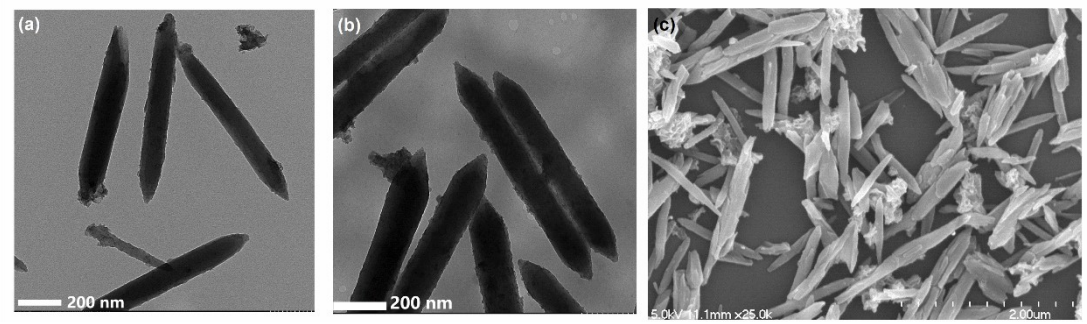

Fig S2. TEM images of (a) $CeNi_{1.6}$Fe-MIL-53 and (b) Ce@$Ni_{1.6}$Fe-MIL-53. (c) SEM image of $Ce_{1.0}Ni_{1.6}$Fe-MIL-53. Scale bars are: (a, b) 200 nm and (c) 2.00 μm resolutions.

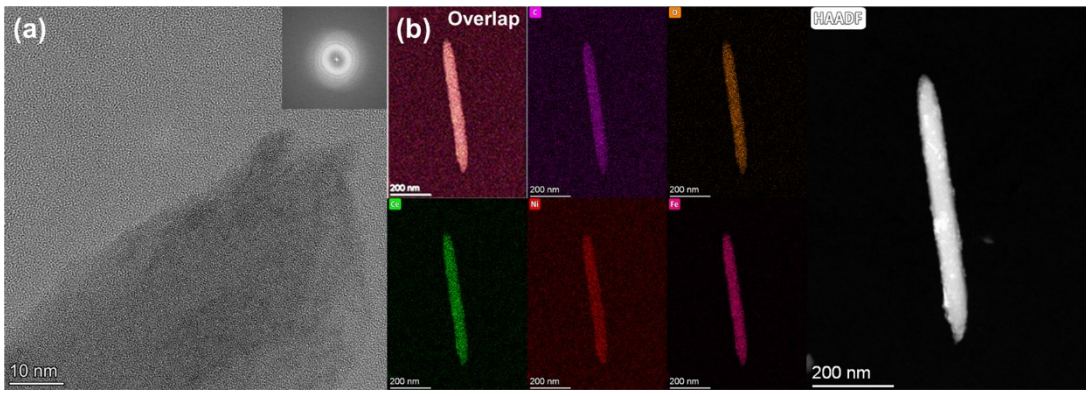

Fig S3. (a) HRTEM images of Ce@NiFe-MOF-5(Insert: Images resulting from fast

Fourier transform of HRTEM images). (b) elements mapping spectrum and HAADF-TEM of $CeNi_{1.6}Fe$-MIL-53.

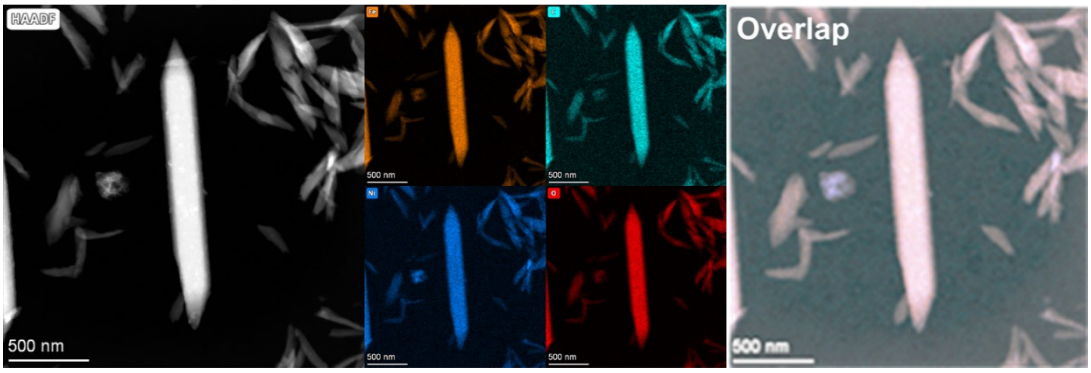

Fig S4. HAADF-TEM and elements mapping spectrum of $Ni_{1.6}Fe$-MIL-53.

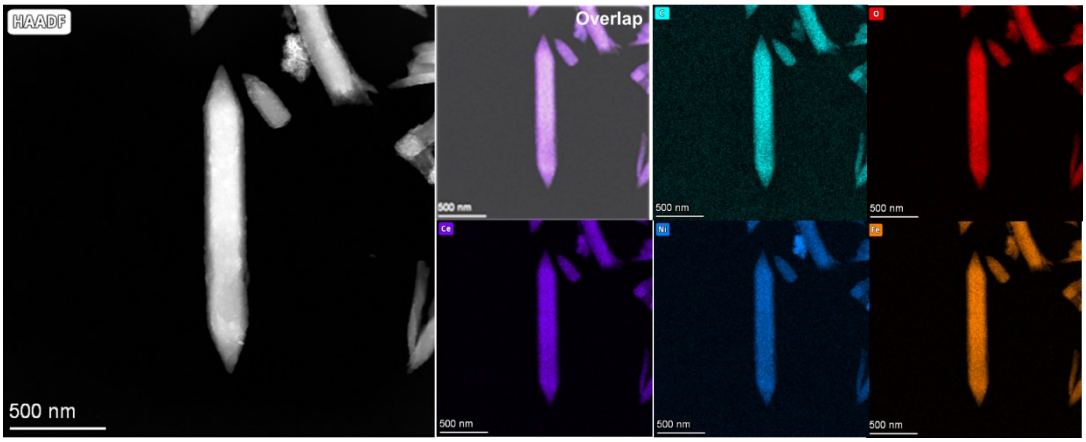

Fig S5. HAADF-TEM and elements mapping spectrum of $Ce@Ni_{1.6}Fe$-MIL-53.

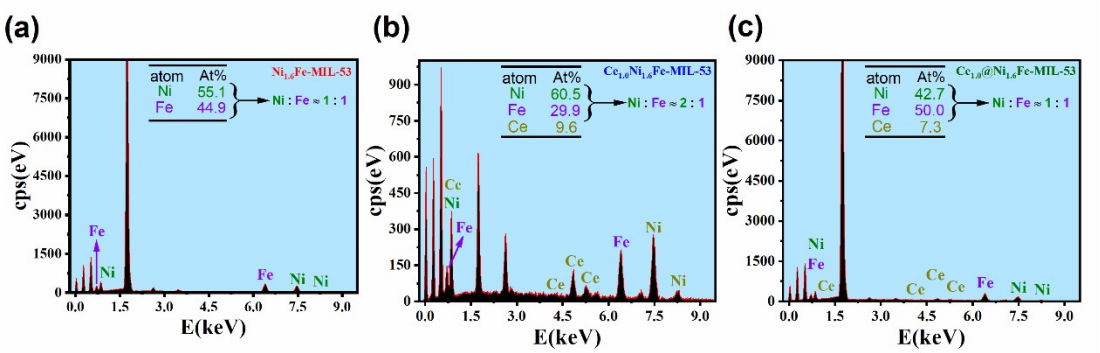

Fig S6. EDS spectrums of (a) $Ni_{1.6}Fe$-MIL-53, (b) $CeNi_{1.6}Fe$-MIL-53 and (c) $Ce@Ni_{1.6}Fe$-MIL-53.

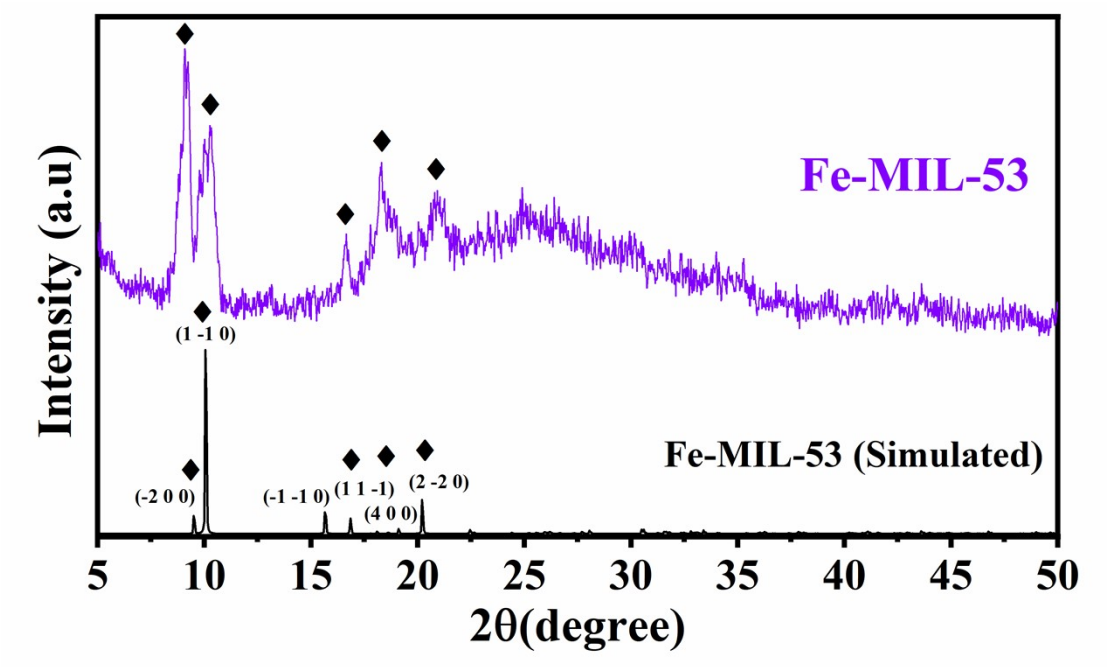

Fig S7. XRD pattern of Fe-MIL-53 and simulated MIL-53.

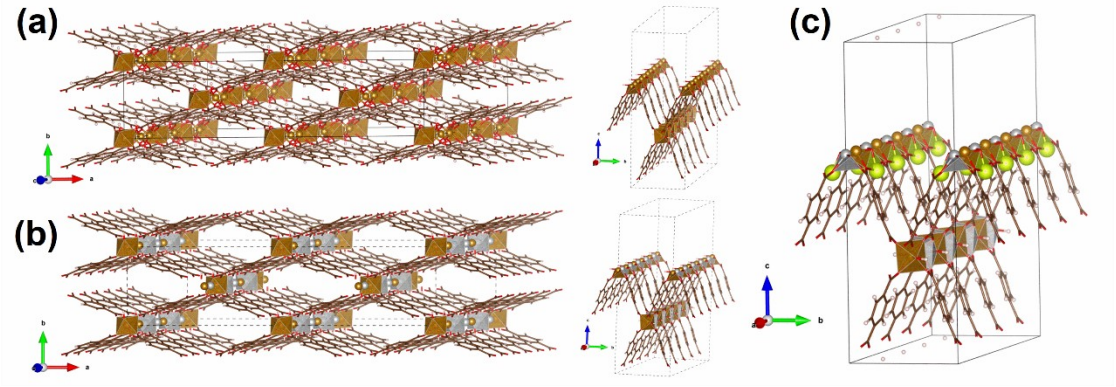

Fig S8. Crystal structure model of (a) Fe-MIL-53, (b) $Ni_{1.6}$Fe-MIL-53 and (c) Ce@$Ni_{1.6}$Fe-MIL-53 (Gray: Ni, Yellow: Fe, Green: Ce, Red: O, Brown: C, Pink: H).

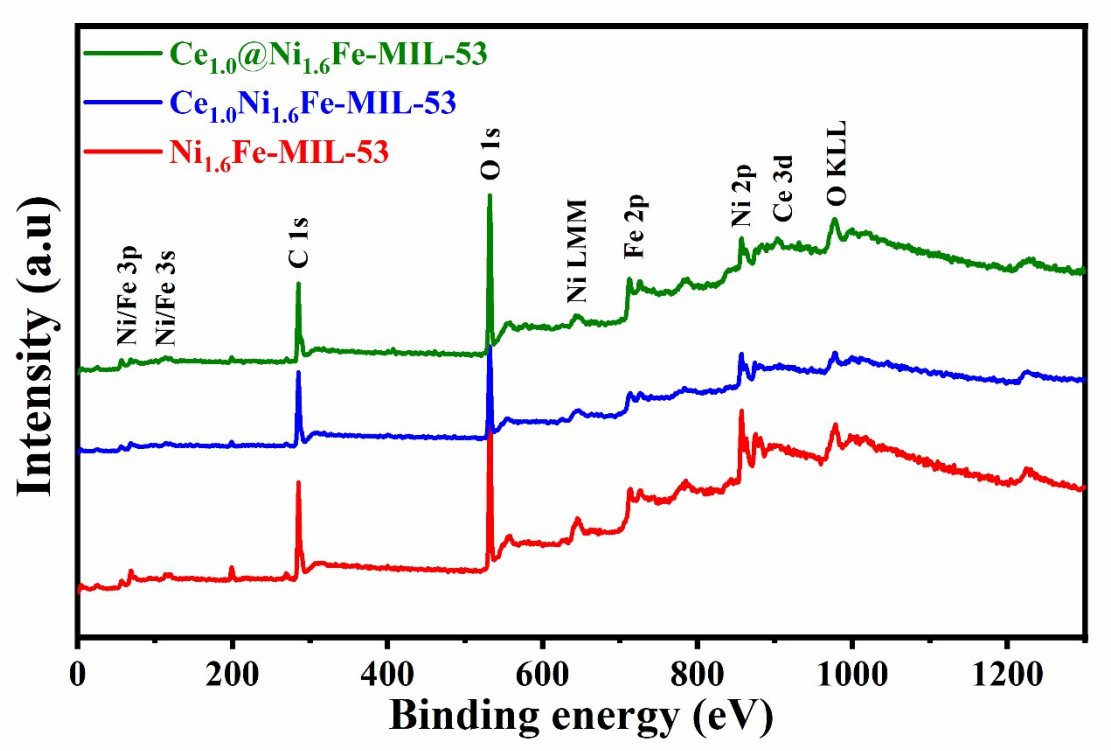

Fig S9. Survey XPS spectrum of $Ni_{1.6}$Fe-MIL-53, $CeNi_{1.6}$Fe-MIL-533 and Ce@$Ni_{1.6}$Fe-MIL-53.

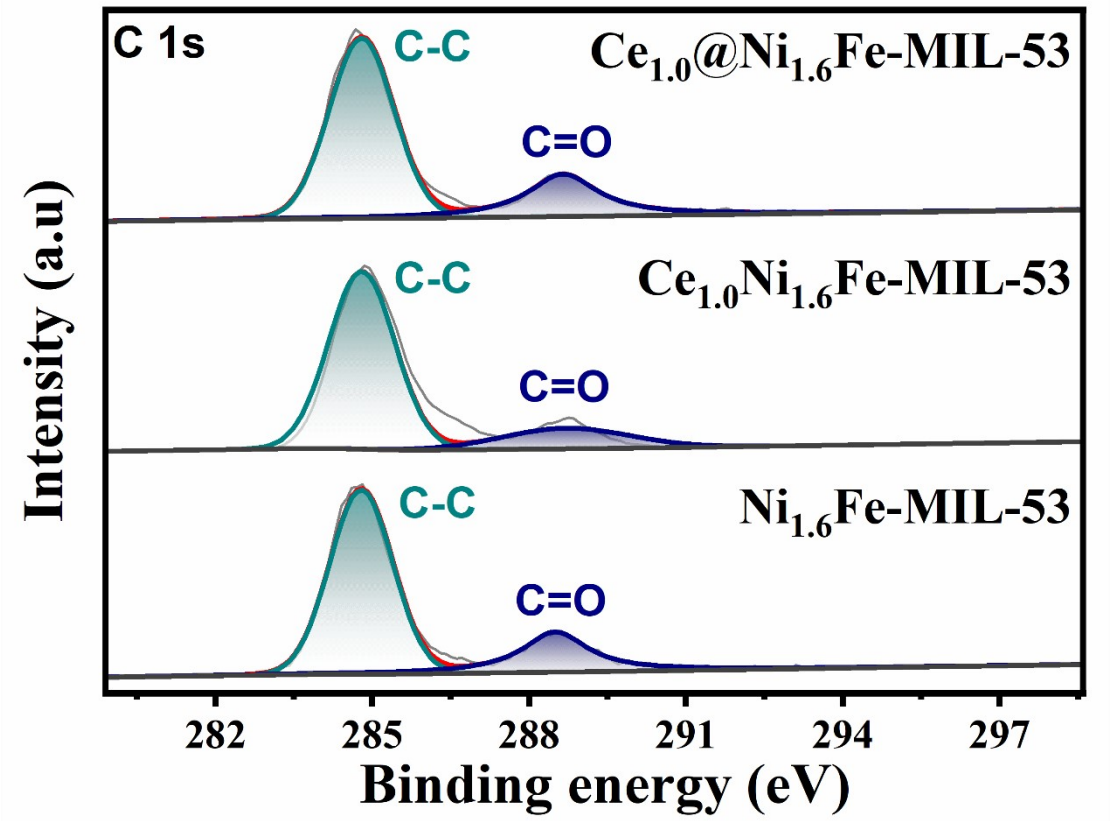

Fig S10. C 1s XPS spectrum of $Ni_{1.6}$Fe-MIL-53, $CeNi_{1.6}$Fe-MIL-533 and Ce@$Ni_{1.6}$Fe-MIL-53.

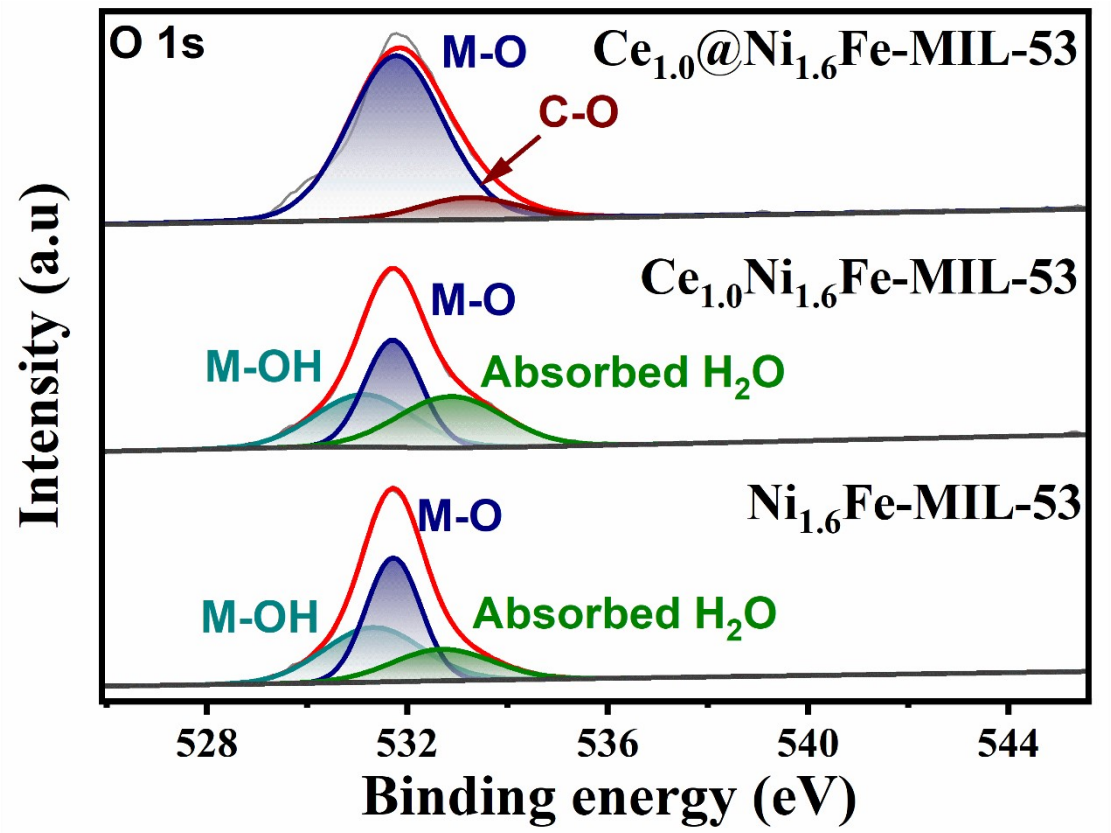

Fig S11. O 1s XPS spectrum of $Ni_{1.6}$Fe-MIL-53, $CeNi_{1.6}$Fe-MIL-533 and Ce@$Ni_{1.6}$Fe-MIL-53.

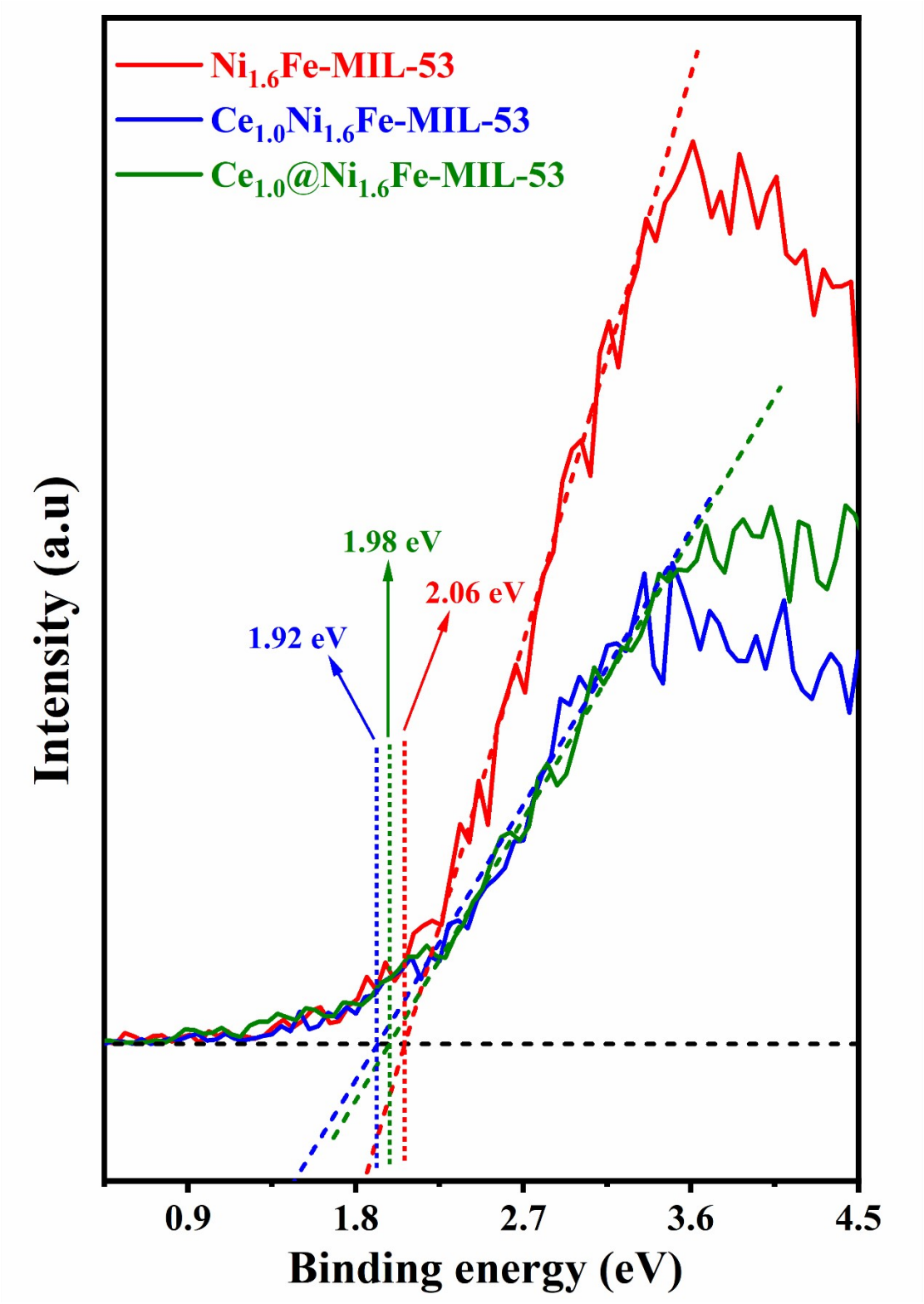

Fig S12. Valence spectra of $Ni_{1.6}$Fe-MIL-53, $CeNi_{1.6}$Fe-MIL-533 and $Ce@Ni_{1.6}$Fe-MIL-53.

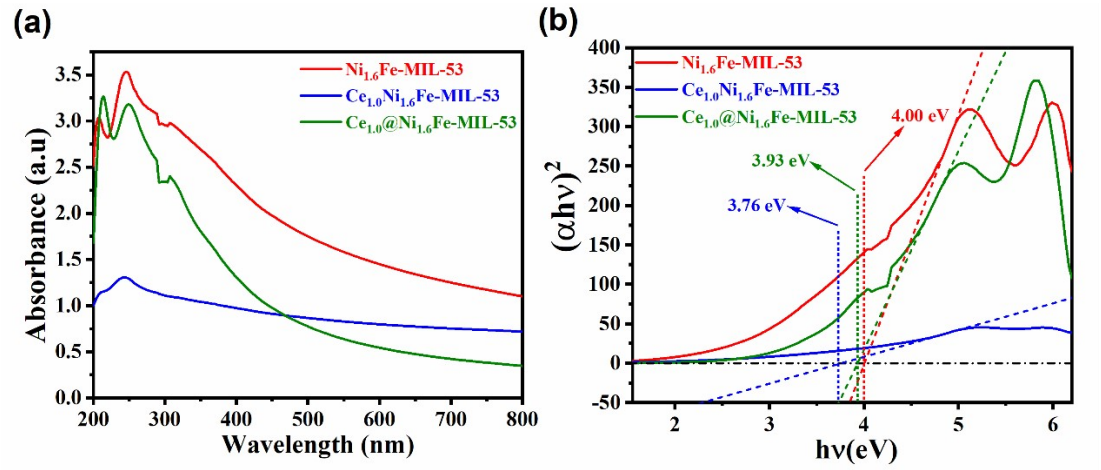

Fig S13. (a) UV–Vis absorption spectra and (b) Tauc plot curves of $Ni_{1.6}$Fe-MIL-53, $CeNi_{1.6}$Fe-MIL-533 and Ce@$Ni_{1.6}$Fe-MIL-53.

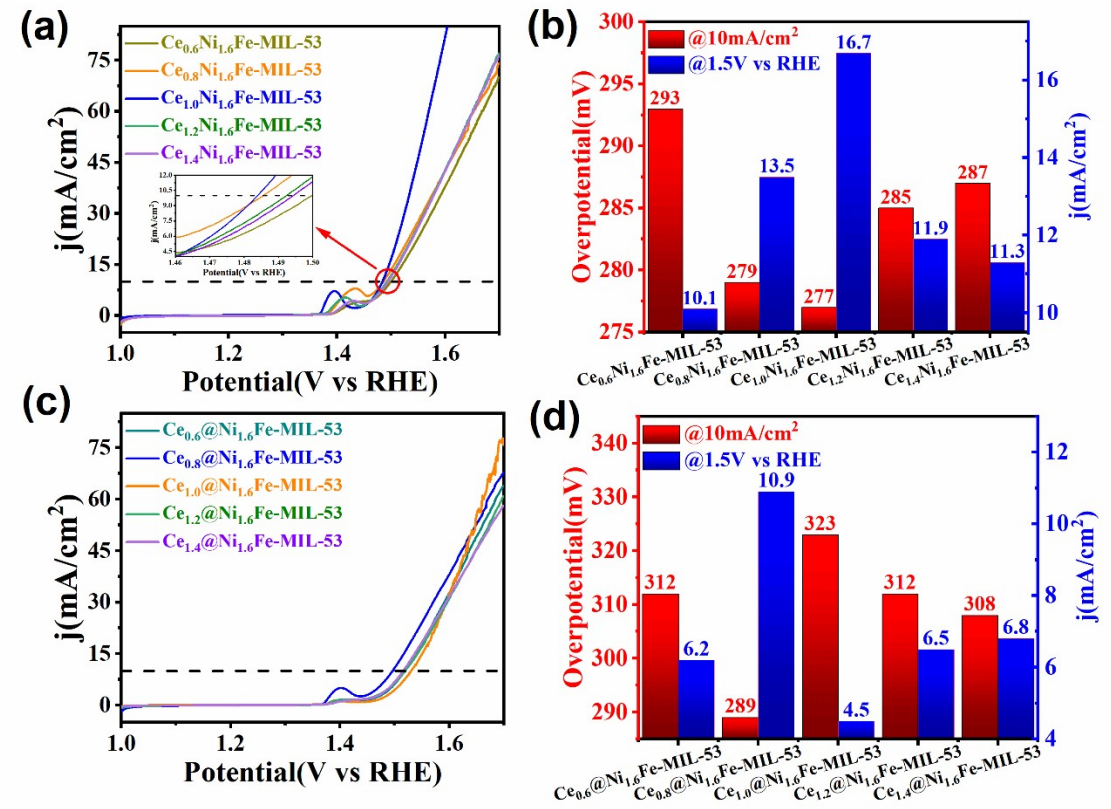

Fig S14. Linear sweep voltammetric OER curves of (a) $Ce_xNi_{1.6}$Fe-MIL-53 and (c) Ce_x@$Ni_{1.6}$Fe-MIL-53 (x = 0.6, 0.8, 1.0, 1.2, 1.4). Over potential and current density of corresponding (b) $Ce_xNi_{1.6}$Fe-MIL-53 and (d) Ce_x@$Ni_{1.6}$Fe-MIL-53 (x = 0.6, 0.8, 1.0, 1.2, 1.4) at 10 mA cm^{-2} and 1.5 V vs RHE, respectively.

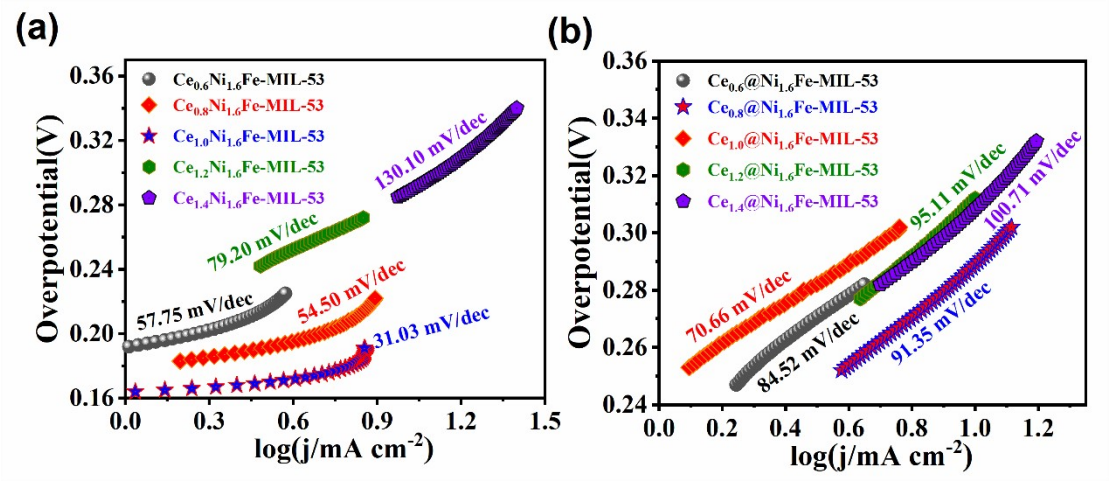

Fig S15. Tafel plots of (a) $Ce_xNi_{1.6}$Fe-MIL-53 and (b) Ce_x@$Ni_{1.6}$Fe-MIL-53 (x = 0.6, 0.8, 1.0, 1.2, 1.4).

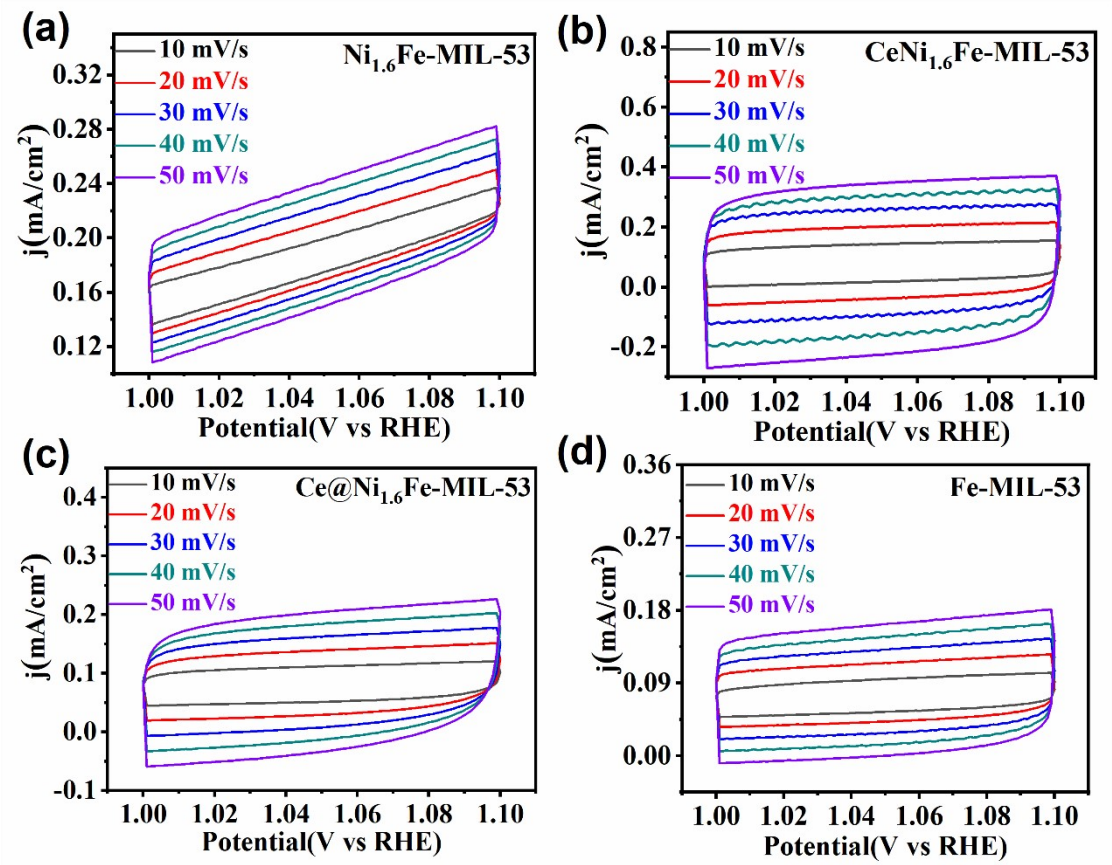

Fig S16. CV curves of (a) $Ni_{1.6}$Fe-MIL-53, (b) $CeNi_{1.6}$Fe-MIL-53, (c) Ce@$Ni_{1.6}$Fe-MIL-53 and (d) Fe-MIL-53 at potential of 1.0 ~ 1.1 V vs RHE from scan rate of 10 mV s^{-1} ~ 50 mV s^{-1}.

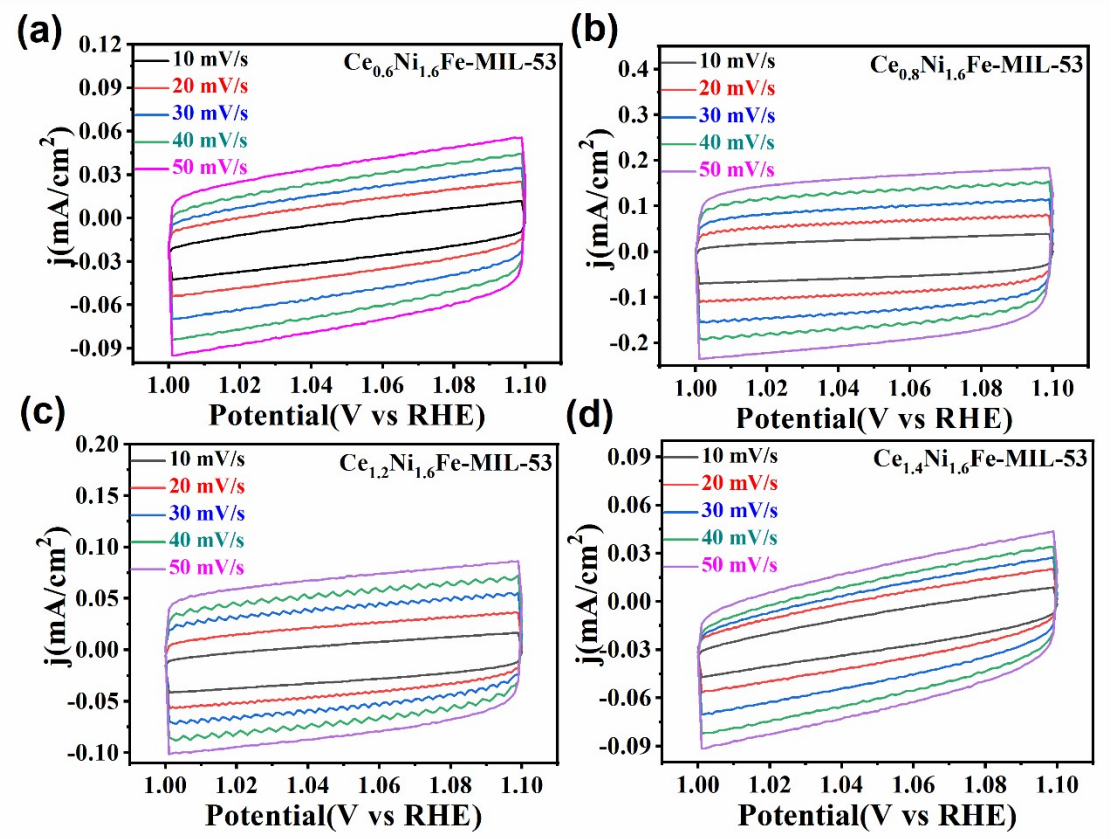

Fig S17. CV curves of (a) $Ce_{0.6}Ni_{1.6}$Fe-MIL-53, (b) $Ce_{0.8}Ni_{1.6}$Fe-MIL-53, (c) $Ce_{1.2}Ni_{1.6}$Fe-MIL-53 and (d) $Ce_{1.4}Ni_{1.6}$Fe-MIL-53 at potential of 1.0 ~ 1.1 V vs RHE from scan rate of 10 mV s^{-1} ~ 50 mV s^{-1}.

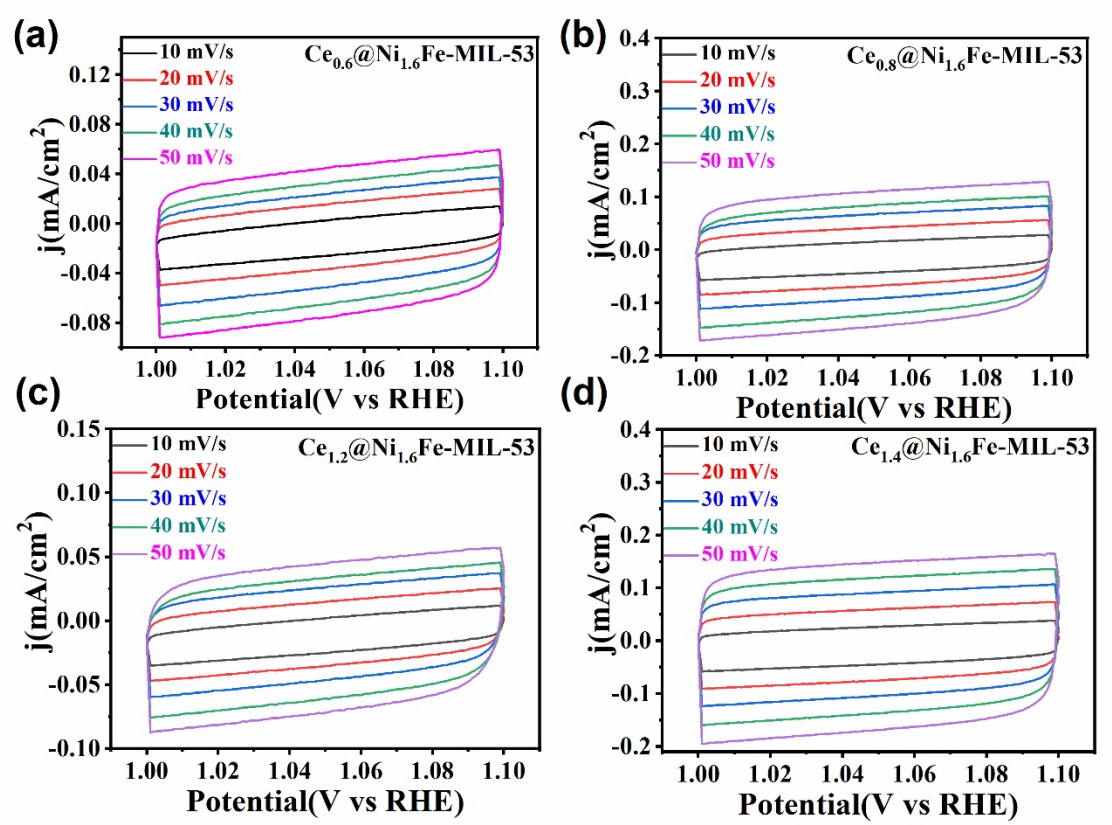

Fig S18. CV curves of (a) $Ce_{0.6}@Ni_{1.6}Fe$-MIL-53, (b) $Ce_{0.8}@Ni_{1.6}Fe$-MIL-53, (c) $Ce_{1.2}@Ni_{1.6}Fe$-MIL-53 and (d) $Ce_{1.4}@Ni_{1.6}Fe$-MIL-53 at potential of 1.0 ~ 1.1 V vs RHE from scan rate of 10 mV s^{-1} ~ 50 mV s^{-1}.

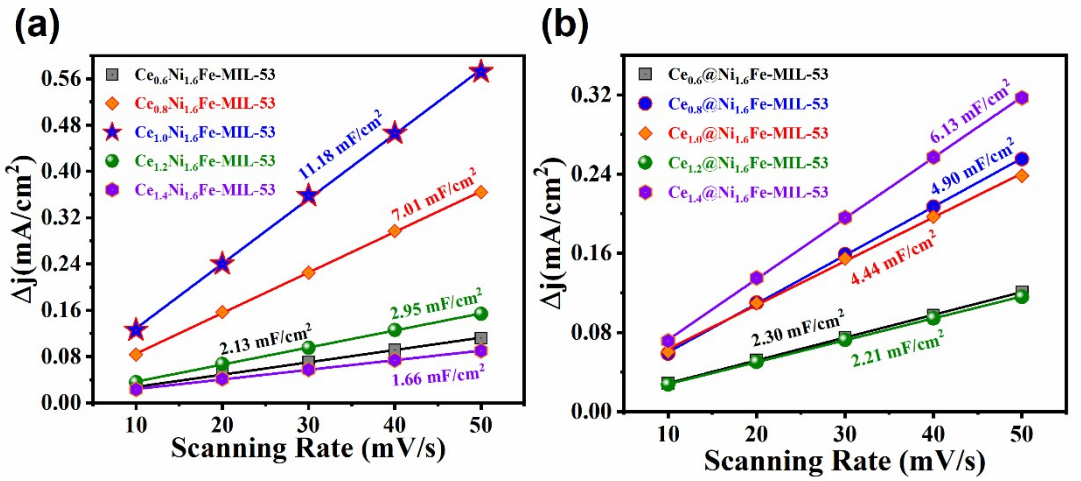

Fig S19. Plots of the current density differences vs scan rate for (a) $Ce_xNi_{1.6}Fe$-MIL-53 and (b) $Ce_x@Ni_{1.6}Fe$-MIL-53 (x = 0.6, 0.8, 1.0, 1.2, 1.4) at 1.05 V in the non-Faradic range, respectively.

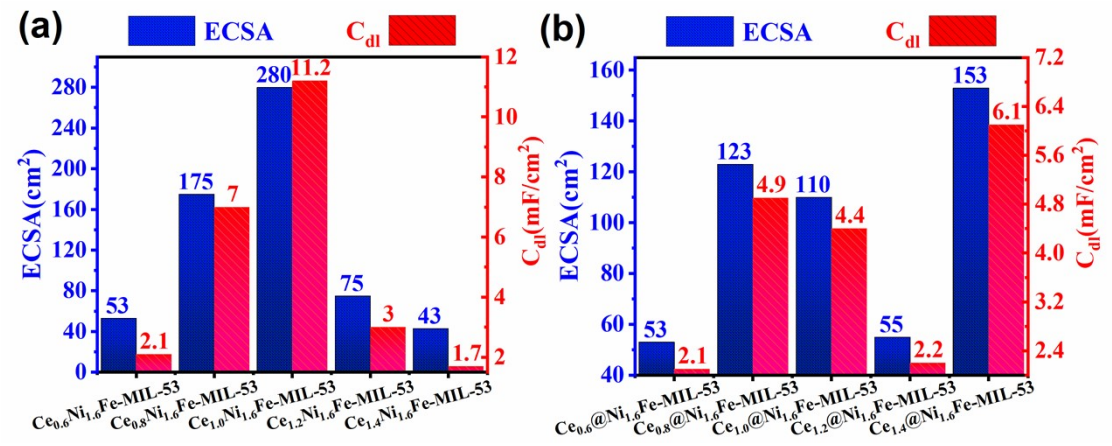

Fig S20. ECSA and C_{dl} value of (a) $Ce_xNi_{1.6}$Fe-MIL-53 and (b) Ce_x@$Ni_{1.6}$Fe-MIL-53 (x = 0.6, 0.8, 1.0, 1.2, 1.4), respectively.

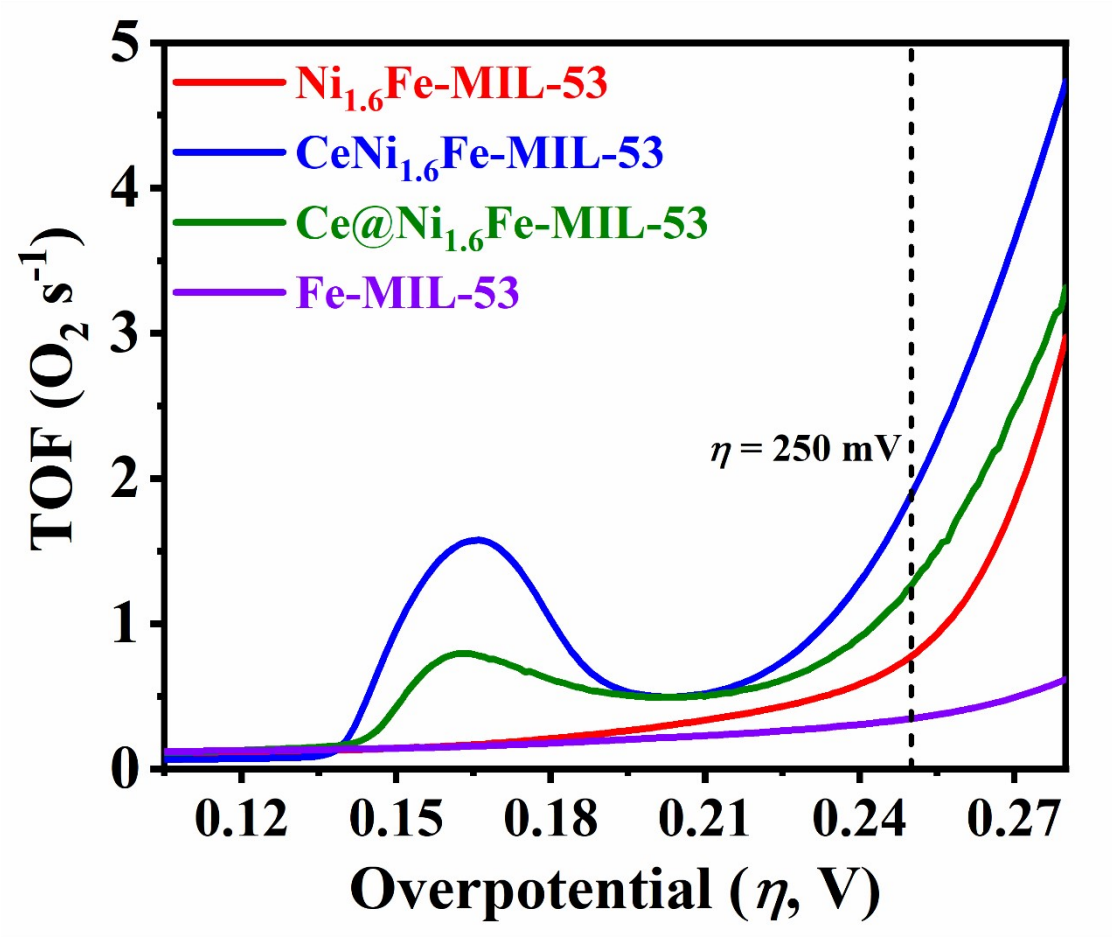

Fig S21. Calculated O_2 TOF values of different electrocatalysts.

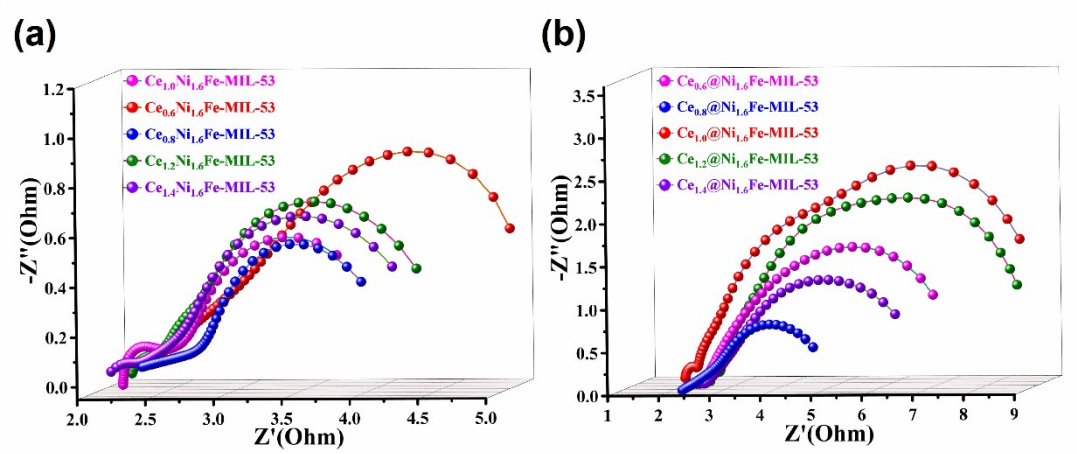

Fig S22. EIS Nyquist plots of (a) $Ce_xNi_{1.6}Fe$-MIL-53 and (b) $Ce_x@Ni_{1.6}Fe$-MIL-53 (x = 0.6, 0.8, 1.0, 1.2, 1.4).

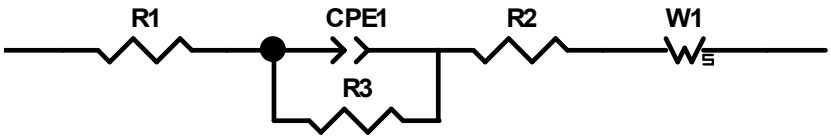

Element	Freedom	Value	Error	Error %
R1	Free(+)	10.96	N/A	N/A
CPE1-T	Free(+)	0.0016393	N/A	N/A
CPE1-P	Free(+)	0.61586	N/A	N/A
R3	Free(+)	2.443	N/A	N/A
R2	Free(+)	12.69	N/A	N/A
W1-R	Free(+)	7.347	N/A	N/A
W1-T	Free(+)	0.18047	N/A	N/A
W1-P	Free(+)	0.49206	N/A	N/A

Fig S23. Electrochemical fitting circuit and circuit parameters for $CeNi_{1.6}Fe$-MIL-53.

Table S1. XPS peak types and corresponding binding energies of C 1s in $Ni_{1.6}$Fe-MIL-53, $CeNi_{1.6}$Fe-MIL-53 and Ce@$Ni_{1.6}$Fe-MIL-53.

Element	Catalyst	C-C	C=O
C	Ce@$Ni_{1.6}$Fe-MIL-53	284.92 eV	288.77 eV
	$CeNi_{1.6}$Fe-MIL-53	284.75 eV	288.70 eV
	$Ni_{1.6}$Fe-MIL-53	284.89 eV	288.60 eV

Table S2. XPS peak types and corresponding binding energies of O 1s in $Ni_{1.6}$Fe-MIL-53, $CeNi_{1.6}$Fe-MIL-53 and Ce@$Ni_{1.6}$Fe-MIL-53.

Element	Catalyst	M-OH	M-O	Absorbed H_2O	C-O
O	Ce@$Ni_{1.6}$Fe-MIL-53	None	531.78 eV	None	533.24 eV
	$CeNi_{1.6}$Fe-MIL-53	531.13 eV	531.71 eV	532.87 eV	None
	$Ni_{1.6}$Fe-MIL-53	531.31 eV	531.72 eV	532.69 eV	None

Table S3. XPS peak types and corresponding binding energies of Ni and Fe 2p in $Ni_{1.6}$Fe-MIL-53, $CeNi_{1.6}$Fe-MIL-53 and Ce@$Ni_{1.6}$Fe-MIL-53.

Element	Catalyst	$2p_{3/2}$	Satellite-1	$2p_{1/2}$	Satellite-2
Ni^{2+}	Ce@$Ni_{1.6}$Fe-MIL-53	856.53 eV	861.99 eV	874.16 eV	881.44 eV
	$CeNi_{1.6}$Fe-MIL-53	856.28 eV	861.79 eV	873.89 eV	880.29 eV
	$Ni_{1.6}$Fe-MIL-53	856.33 eV	861.74 eV	874.04 eV	879.98 eV
Fe^{3+}	Ce@Ni1.6Fe-MIL-53	712.14 eV	717.62 eV	725.44 eV	732.58 eV
	CeNi1.6Fe-MIL-53	712.52 eV	718.40 eV	725.51 eV	733.42 eV
	Ni1.6Fe-MIL-53	712.33 eV	718.42 eV	725.80 eV	732.79 eV

Table S4. XPS peak types and corresponding binding energies of Ce 3d in $CeNi_{1.6}$Fe-MIL-53 and Ce@$Ni_{1.6}$Fe-MIL-53.

Catalyst	Ce^{3+}		Ce^{4+}	
	$3d_{5/2}$	$3d_{3/2}$	Characteristic peak	$3d_{3/2}$
$CeNi_{1.6}$Fe-MIL-53 (Ce^{3+}: 43.49%, Ce^{4+}:56.51%)	880.65 eV 891.05 eV	897.65 eV 903.65 eV	873.75 eV	911.35 eV 918.65 eV
Ce@$Ni_{1.6}$Fe-MIL-53 (Ce^{3+}: 49.33%, Ce^{4+}:50.67%)	881.46 eV 887.21 eV	895.67 eV 903.59 eV	874.13 eV	909.67 eV 921.74 eV

* Only $3d_{3/2}$ peaks are taken into the calculation for accuracy as the $3d_{5/2}$ region is influenced by Ni 2*p* spectra even after the removal of overlapping Ni peaks [3].

Table S5. Comparison of activity between Ce@NiFe-MOF-5 and other Ce-doped catalysts.

Catalysts	OER Activity		References
	η_{10} (mV)	Tafel slope (mV dec^{-1})	
$CeNi_{1.6}Fe$-MIL-53	277	31.03	This work
CSCNF1	277	54.1	[4]
5%Ce-CoAl LDH@MoS_2	278	65.7	[5]
CeO_2-Co_3O_4/CF	285	70	[6]
Ce-$Co(PO_3)_2$@NF–1	286	64.3	[7]
Ce-doped CoMoP/MoP@C	287	74.4	[8]
$NiCeO_x$	295	66	[9]
CeFeCoP/NF	298	114	[10]
$Ce_{0.21}$@$Co(OH)_2$	300	72	[11]
$Ce_{0.2}MnFe_{1.8}O_4$	310	31	[12]
Ce-NiO-E	382	118.7	[13]
Ce-NiO-L	426	131.6	
$CeCu_3Ru_4O_{12}$	311	119	[14]
CeO_2/Co_4N	318	80	[15]
CoO-CeO_2	319	63	[16]
$Co_{0.9}Ce_{0.1}O_x$	320	104.7	[17]
NiS/CeS/SSS	289	44	[18]
CoO/CeO_2	291	84	
Ag-CeO_2-Co_3O_4/C	340	130.1	[19]
Ce(3)-Co_3O_4	369	56	[20]
Ce-CMO-18%	378	86	[21]
Ir@CeO_2	379	93.4	[22]
LCC4	380	80	[23]
Ce-$LaCoO_3$(5.6%)	450	112	[24]
20CeO_2/Co–Bi	453	120	[25]

References

1. C. C. L. McCrory, S. Jung, I. M. Ferrer, S. M. Chatman, J. C. Peters and T. F. Jaramillo, *J. Am. Chem. Soc.*, 2015, **137**, 4347-4357.

2. L. Yaqoob, T. Noor, N. Iqbal, H. Nasir, N. Zaman and K. Talha, *J. Alloys Compd*, 2021, **850**, 156583.

3. M. Liu, K. A. Min, B. Han and L. Y. S. Lee, *Adv. Energy Mater.*, 2021, **11**, 2101281.

4. C. B. Njoku and R. J. Kriek, *Electrocatalysis*, 2020, **11**, 628-641.

5. M. K. Rong, Y. Mo, S. W. Zhou, X. Ma, S. Wang, Z. F. Cao and H. Zhong, *Int. J. Hydrog. Energy*, 2022, **47**, 1644-1655.

6. X. Yang, Z. X. Tao, Y. M. Wu, W. Lin and J. Zheng, *J. Alloys Compd*, 2020, **828**, 154394.

7. Y. Y. Yang, Y. L. Xiong, Q. Zhou, J. Y. Yang, D. L. Qian and Z. A. Hu, *Mater Sci Eng B Solid State Mater Adv Technol*, 2023, **290**, 116344.

8. T. Y. Chen, Y. Y. Fu, W. H. Liao, Y. Q. Zhang, M. Qian, H. J. Dai, X. F. Tong and Q. H. Yang, *Energy Fuels*, 2021, **35**, 14169-14176.

9. J. Yu, Q. Cao, Y. B. Li, X. Long, S. H. Yang, J. K. Clark, M. Nakabayashi, N. Shibata and J. J. Delaunay, *ACS Catal.*, 2019, **9**, 1605-1611.

10. L. H. Shen, S. H. Tang, L. M. Yu, Q. K. Huang, T. L. Zhou, S. Yang, H. L. Yu, H. X. Xiong, M. J. Xu, X. Zhong and L. Zhang, *J Solid State Chem*, 2022, **314**, 123434.

11. Y. N. Zhou, R. Y. Fan, S. Y. Dou, B. Dong, Y. Ma, W. L. Yu, M. X. Li, Y. L. Zhou, C. G. Liu and Y. M. Chai, *J. Energy Chem*, 2021, **59**, 299-305.

12. T. Pandiarajan, S. Ravichandran and L. J. Berchmans, *Rsc Advances*, 2014, **4**, 64364-64370.

13. W. Gao, Z. Xia, F. Cao, J. C. Ho, Z. Jiang and Y. Qu, *Adv. Funct. Mater.*, 2018, **28**, 1706056.

14. W. Liu, K. Kawano, M. Kamiko, Y. Kato, Y. Okazaki, I. Yamada and S. Yagi, *Small*, 2022, **18**, e2202439.

15. X. P. Sun, Y. H. Zhang, Y. Xiao, Z. Q. Li, L. Z. Wei, G. Yao, H. L. Niu and F. C.

Zheng, *Inorg. Chem.*, 2022, **61**, 14140-14147.

16. X. N. Ren, F. Hou, F. Y. Wang, X. W. Zhang and Q. F. Wang, *Int. J. Hydrog. Energy*, 2018, **43**, 22529-22537.

17. L. L. Pan, Q. Q. Wang, Y. D. Li and C. J. Zhang, *J Catal*, 2020, **384**, 14-21.

18. H. Z. Liu, H. Duan, J. Yu, C. Qiu, R. X. Yu, J. Q. Gao, S. M. Li, X. J. Du, Z. C. Si and S. H. Yang, *ACS Mater. Lett*, 2022, **4**, 2572-2578.

19. T. Li, Z. He, X. Liu, M. Jiang, Q. Liao, R. Ding, S. Liu, C. Zhao, W. Guo, S. Zhang and H. He, *Surf. Interfaces*, 2022, **33**, 102270.

20. J. M. Zhou, H. Y. Zheng, Q. J. Luan, X. B. Huang, Y. Li, Z. S. Xi, G. L. Lu, L. W. Xing and Y. Q. Li, *Sustain. Energy Fuels*, 2019, **3**, 3201-3207.

21. X. Chen, F. Han, X. Chen, C. Zhang and W. Gou, *Catalysts*, 2022, **12**, 1122.

22. M. Akbayrak and A. M. Önal, *J. Electrochem. Soc.*, 2022, **169**, 076511.

23. D. W. Ji, C. H. Liu, Y. H. Yao, L. L. Luo, W. C. Wang and Z. D. Chen, *Nanoscale*, 2021, **13**, 9952-9959.

24. J. Qian, T. Wang, Z. Zhang, Y. Liu, J. Li and D. Gao, *Nano Energy*, 2020, **74**, 104948.

25. X. M. Zhou, S. J. Guo, Q. R. Cai and S. M. Huang, *Nanoscale Adv.*, 2019, **1**, 3686-3692.